6. Oxygen chemisorption on Au(110)-(1×2)

The growing interest in the field of catalysis on gold, especially CO oxidation catalysis [Bo99, Bo00], has also revived the interest in the gold-oxygen interaction on gold single-crystal surfaces, although the crucial step of catalytic oxidations, the spontaneous cleavage of the O-O bond, could not be observed on extended gold samples. However, for model studies which intend to elucidate the mechanism of these catalytic reactions it is desirable to generate chemisorbed oxygen phases also on single-crystal surfaces. In order to achieve oxygen chemisorption on Au(110)-(1×2), we activated the system dioxygen/gold by bombardment of physisorbed O_2 with electrons (500 eV), a method that we described in Chapter 5 in detail. In the present chapter, we first present and discuss our experimental and simulated thermal desorption spectra. The remaining sections will be devoted to results obtained with techniques such as UV photoelectron spectroscopy (UPS), low-energy electron diffraction (LEED), work function measurements ($\Delta\varphi$), and reactive thermal desorption measurements (RTDM).

The chemisorbed oxygen phases were prepared according to Chapter 5 by electron stimulated chemisorption as follows: Dioxygen[1] was condensed on the gold surface at 28 K. Thereafter, the dioxygen layer was bombarded for 3 minutes with electrons of 500 eV energy and a primary electron current density of 3.9 mA/cm^2. Approximately 50 % of the condensed oxygen was converted to chemisorbed oxygen. Different coverages of chemisorbed oxygen were obtained by varying the initial coverage of physisorbed (or condensed) oxygen.

6.1. Thermal desorption measurements

6.1.1. Thermal desorption states and coverages

Fig. 6.1 shows a representative series of oxygen thermal desorption spectra, taken with a heating rate of 2.015 (± 0.002) K/s for coverages ranging from 0.04 to 1.80 ML. Two desorption states were successively occupied: first, the high-temperature state β_2 appeared around 550 K, followed by a further desorption state β_1 around 490 K. (The low-temperature range, which is dominated by the desorption of remaining physisorbed O_2, is not displayed in Fig. 1.)

A saturated β_2 peak corresponds to a coverage of 1.68×10^{15} O atoms per cm^2 as determined by the method described in Section 4.1.6. Since the substrate surface exposes (ideally) 1.696×10^{15} gold atoms per cm^2, this value corresponds to a relative coverage of 0.99 oxygen atoms per surface gold atom. Therefore, β_1 must stem either from oxygen atoms below the surface, i.e., it is subsurface or (surface-near) bulk oxygen, or from a gold oxide with variable stoichiometry. The former interpretation is suggested by a comparison with the O/Ag system, for which a dissolved bulk oxygen species is observed in the case

[1] Oxygen gas 4.8, purity > 99.998%, Messer Griesheim, Germany.

of oxygen adsorption on silver at high temperatures and pressures [Re91, Re91a, Ba93, Ba93a, Sc94, Sc95, Ba96, He96]. However, oxygen atoms implanted in the bulk of the Au(110)-(1×2) crystal by O^+ / O_2^+ ion bombardment desorb above 700 K and do not react with carbon monoxide (CO), as shown in Chapter 7. In contrast, no oxygen desorption occurred above 650 K in our experiments. This observation, together with the fact that both β_1 and β_2 react eagerly with CO (see Chapter 11), excludes the existence of a bulk oxygen species produced by electron bombardment of physisorbed O_2. The assignment of β_1 to subsurface oxygen is equally unlikely since β_1 does not lower the work function, as demonstrated in Section 6.5. Therefore, we favour the identification of β_1 with a gold oxide species. As shown below, there is evidence for attractive interactions between the chemisorbed oxygen atoms, resulting in the formation of islands (see Section 6.2). We may therefore also expect the formation of three-dimensional aggregates of gold oxide at high oxygen loading.

Within the error of the coverage measurement, the saturated β_2 peak corresponds to monolayer coverage. In the following, we use the phenomenological monolayer definition and consider the saturation coverage of β_2 as $\Theta \equiv 1$ ML.

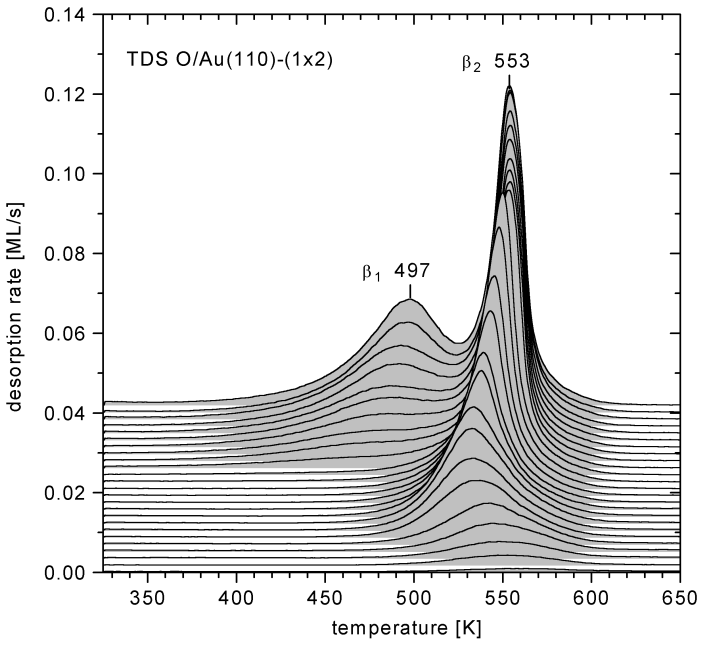

Fig. 6.1: Set of thermal desorption spectra of chemisorbed oxygen on Au(110)-(1×2), taken with a heating rate of 2.015 K/s. The different initial coverages of chemisorbed oxygen were prepared by irradiation of physisorbed oxygen adlayers on Au(110)-(1×2) with electrons as described in Chapter 5. The spectra correspond to the following initial coverages (in ML): 0.04; 0.09; 0.14; 0.22; 0.31; 0.43; 0.52; 0.62; 0.66; 0.69; 0.71; 0.78; 0.84; 0.93; 1.00; 1.07; 1.13; 1.19; 1.28; 1.39; 1.45, 1.54; 1.66; 1.68; 1.80. See text for the details.

6.1.2. Desorption kinetics, activation energies, and frequency factors

In the low coverage range ($\Theta_0 < 0.5$ ML), the β_2 desorption maxima shift to lower temperatures with increasing initial coverages. This behaviour, which is typical of a second-order desorption, suggests the existence of chemisorbed oxygen *atoms* with their recombination as the rate-limiting step of the desorption process. We will determine the desorption order by line shape analysis further below. Most remarkably, the β_2 peak shifts back to higher temperatures as the oxygen coverage exceeds ≈ 0.5 ML; the β_2 leading edges even cross. Furthermore, the peakwidth is increasingly reduced, i.e., the desorption occurs within a much smaller temperature interval than usual. The shape of the high-coverage spectra, especially the steepness of their leading edges, suggests the operation of an autocatalytic mechanism which accelerates the desorption process in addition to the effect of the temperature increase.

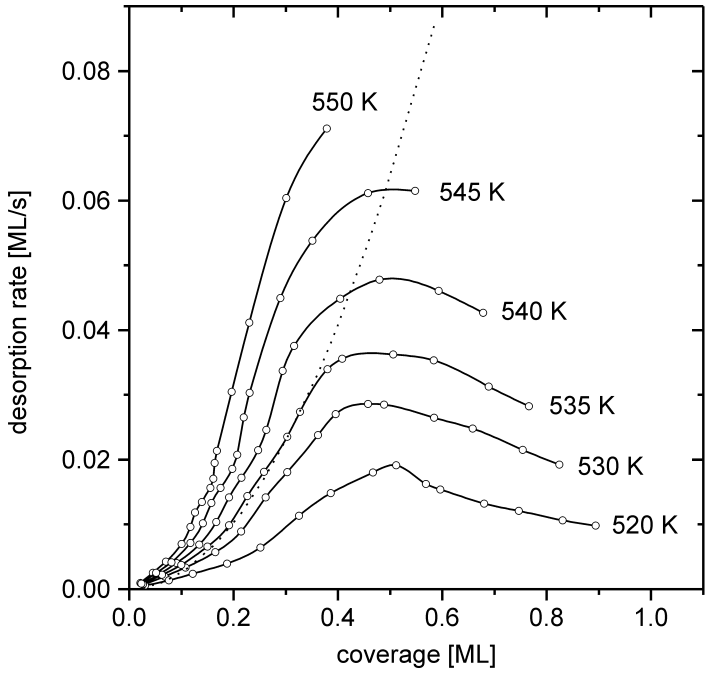

Fig. 6.2: TDS O/Au(110)-(1×2). Plot of the isothermal desorption rate, $R_{des}(\Theta)_T$, vs. coverage, Θ, for the spectra in Fig. 6.1. Clearly, the rate is *not* a monotonous function of coverage, in contrast to the prediction of the Polanyi-Wigner equation (Eq. 4.1), which is represented by the dotted line for the following parameters: n = 2, T = 535 K, E_{des} = 141 kJ/mol, and $\nu_2 = 1.8\times10^{13}$ s^{-1} ML^{-1} (see Table 6.1 further below).

For fixed temperature, the isothermal desorption rate $R_{des}(\Theta)_T$ should, according to the Polanyi-Wigner equation (Eq. 4.1), increase monotonously with Θ^n if the other parameters E_{des}, ν_n, and n are independent of Θ. In Fig. 6.2, $R_{des}(\Theta)_T$ (extracted from the submonolayer spectra in Fig. 6.1) is plotted vs. Θ for several constant temperatures. The curves are parabolic up to ≈ 0.35 ML, indicating a desorption order of ≈ 2. At higher coverages, the curves flatten and reach a maximum around 0.5 ML, whereafter $R_{des}(\Theta)_T$ de-

creases despite increasing coverage. Clearly, the chemisorbed oxygen inhibits its own desorption above 0.5 ML, a behaviour that is not explained by Eq. 4.1 (at least not for fixed activation parameters). Obviously, the desorption kinetics of the β_2 state requires a more detailed investigation.

In the following, we extract E_{des}, ν_n, and n from the 'well-behaved' low-coverage spectra. Thereafter, we analyse spectra taken with different heating rates in order to obtain similar information for the high-coverage range. In Section 6.2, we finally suggest a model for a desorption mechanism that is consistent with all observations reported in this chapter.

ACTIVATION ENERGY, FREQUENCY FACTOR, AND ORDER OF DESORPTION AT LOW COVERAGES ($\Theta \leq 0.35$ ML) – In the low-coverage range, the desorption process follows a second-order kinetics. This fact is demonstrated in Fig. 6.3, where $\ln R_{des}(\Theta)_T$ is plotted vs. $\ln \Theta$ for various temperatures. If the Polanyi-Wigner equation (Eq. 4.1) applies in this coverage range, we expect a straight line with a slope equal to the desorption order n (see Section 4.1.3). The plots are indeed nearly linear, and from the best linear fits we obtain values of n that are close to two (between 1.8 and 2.0).

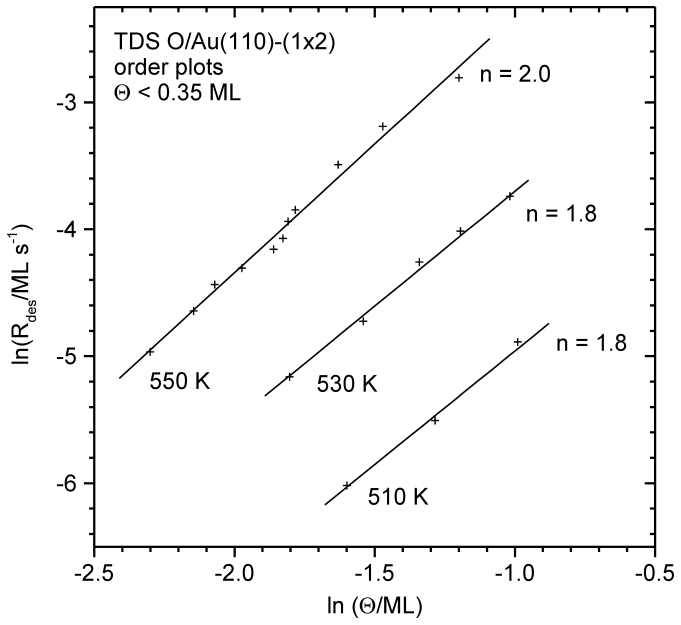

Fig. 6.3: Order plots for the low-coverage range (< 0.35 ML) of the spectra in Fig. 6.1, confirming second-order desorption.

With the desorption order n known, we are able to evaluate the other activation parameters from a plot of $\ln (R_{des}/\Theta^n)$ vs. 1/T (Arrhenius plot). According to the Polanyi-Wigner equation (Eq. 4.1), a correct choice of n leads to a straight line with the slope E_{des}/R and

an intercept that is a function of ν_n. (For a wrong choice of n, the plot deviates characteristically from linearity, especially around the desorption maximum, as shown in Figs. 5.3 and 6.5a). In Fig. 6.4, these plots where drawn for two different initial coverages Θ_0, viz., 0.22 and 1.0 ML. For the low-coverage spectrum, a straight line and the parameters E_{des} = 141 kJ/mol and $\nu_2 = 1.8\times10^{13}$ $s^{-1}ML^{-1}$ (or 1.1×10^{-2} cm^2s^{-1}) were obtained. In contrast, the high-coverage spectrum leads to a plot that deviates strongly from linearity for any choice of n. Only for coverages below 0.35 ML the curve for Θ_0 = 1.0 ML nearly coincides with the other curve in Fig. 6.4. Obviously, a change in the desorption mechanism occurs at this coverage.

The Arrhenius plots for the high-coverage range deviate from linearity for *any* choice of the desorption order, n. This fact is demonstrated in Fig. 6.5, which shows a range of Arrhenius plots with different assumed desorption orders for a low-coverage and a high-coverage spectrum. As expected, the plots for the low-coverage spectrum (Θ_0 = 0.20 ML) are approximately linear only for n ≈ 2. Other values of n lead to deviations from linearity as predicted for incorrect desorption orders (see Section 4.1.3). From the best linear fit, a frequency factor $\nu_2 = 1.4\times10^{13\pm0.3}$ s^{-1} (or, related to the absolute coverage, $6.0\times10^{-3\pm0.3}$ cm^2s^{-1}) and a desorption activation energy E_{des} = 140 ± 3 kJ/mol were calculated. In contrast, the plots for the high-coverage spectrum (Θ_0 = 0.89 ML) show that linearity is obtained for none of the desorption orders (Fig. 6.5b).

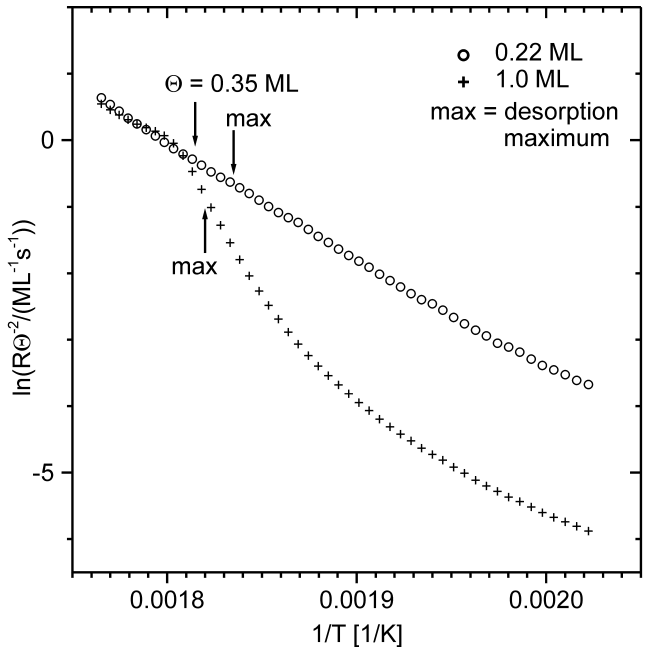

Fig. 6.4: Second-order Arrhenius plots for initial coverages of 0.22 ML and 1.0 ML. The straight line in the low-coverage limit confirms the order n = 2 and provides the other activation parameters E_{des} and ν_2 (see Table 6.1 further below), whereas the high-coverage curve proves the deviation from the Polanyi-Wigner equation (Eq. 4.1) for Θ > 0.35 ML. The vertical bars correspond to the temperatures of maximum desorption. The plot should be linear especially in the vicinity of this point if the correct desorption order was chosen.

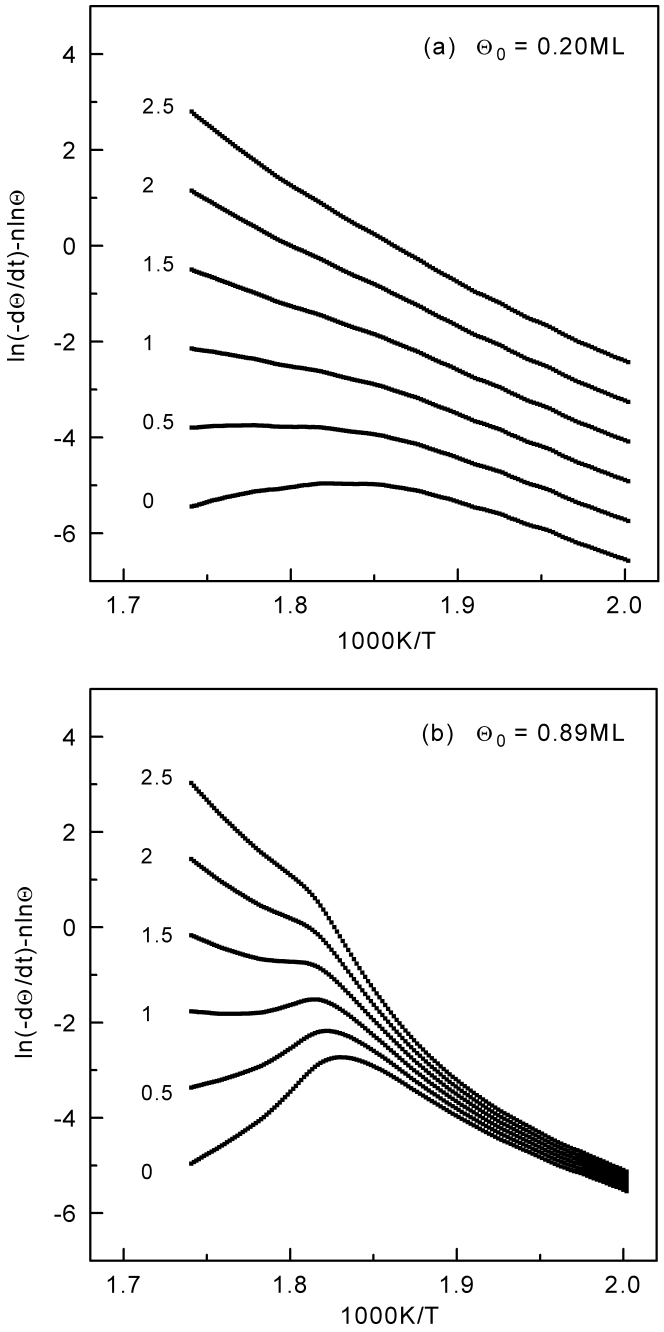

Fig. 6.5. TDS O/Au(110)-(1×2). Arrhenius plots for initial coverages of (a) 0.20 ML and (b) 0.89 ML. Assumed desorption orders between 0 and 2.5 as indicated.

ACTIVATION ENERGY, FREQUENCY FACTOR, AND ORDER OF DESORPTION AT HIGH COVERAGES (0.35 ML < Θ < 1.0 ML) – Desorption activation parameters for higher initial coverages than 0.35 ML can conveniently be obtained by a variation of the TDS heating rate (HRV in abbreviation) at constant initial coverages. The advantage of this method, especially in cases of complex desorption kinetics, is that it considers only one point of each spectrum, viz., the temperature of maximum desorption, $T_{max} \equiv T(R_{max})$, which is a function of the heating rate β. Hence, the data evaluation is carried out for a constant coverage (namely, the coverage at the desorption maximum, $\Theta_{max} \equiv \Theta(T_{max})$), and should remain unperturbed by the coverage-dependence of the activation parameters or changes in the desorption mechanism.

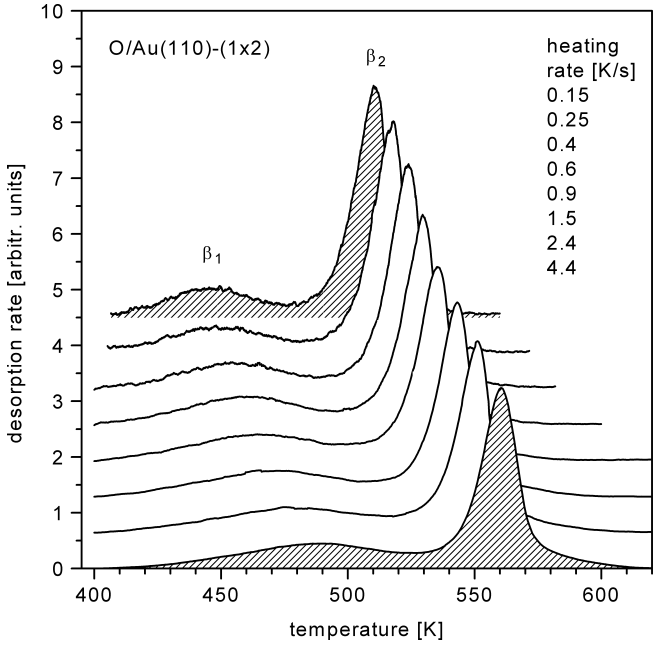

Fig. 6.6: Set of TD spectra with a constant initial coverage of 1.45 ML, but varying heating rate as indicated. With increasing heating rate, the β_1 peak broadens, in contrast to β_2.

The heating rate variation, combined with a quantitative analysis of the spectra as described in Section 4.1.3 was carried out for initial coverages, Θ_0, of 0.45 ML and 1.45 ML. The instantaneous coverages at the maximum of β_2, Θ_{max}, were 0.23 ML and 0.43 ML. Only the TD spectra for the HRV at Θ_0 = 1.45 ML are displayed in Fig. 6.6. In agreements with Eq. 4.11, plots of $\ln(\tilde{T}_{max}^2 / \tilde{\beta})$ vs. $1/T_{max}$ as shown in Fig. 6.7 are linear and allow to extract desorption energies $E_{des}(\Theta_{max})$ and frequency factors $\nu_n(\Theta_{max})$ from slope and intercept. The respective data are summarized in Table 6.1. The β_1 peak was analysed assuming first-order kinetics (since the desorption maxima remain at nearly constant temperature), whereas second-order kinetics was assumed in the case of β_2. (The choice of the desorption order affects only the frequency factor, not the desorption energy.)

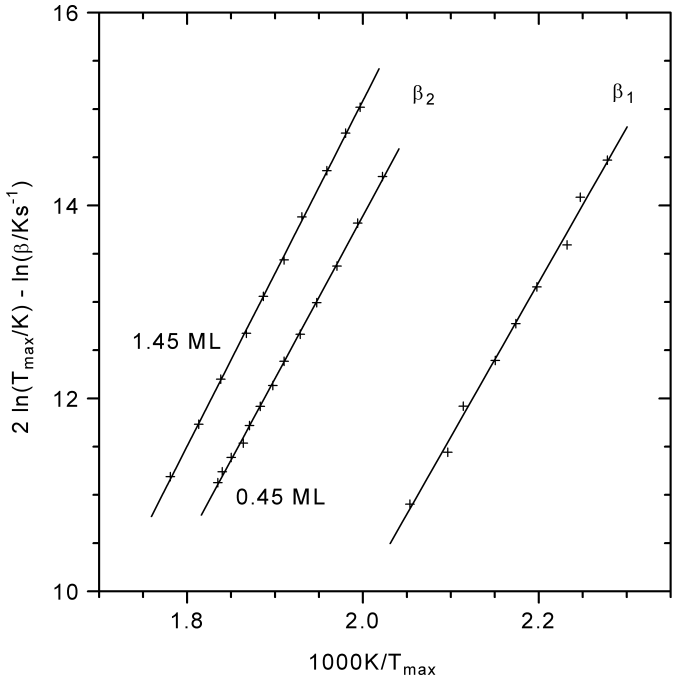

Fig. 6.7: Plots of $\ln(\tilde{T}_{max}^2/\tilde{\beta})$ vs. $1/T_{max}$ for the desorption maxima β_1 and β_2 at initial coverages of 0.45 ML and 1.45 ML. The desorption activation parameters were determined according to Eq. 4.11 from the slope and intercept of the best linear fits and are displayed in Table 6.1.

Θ_0 [ML]	E_{des} [kJ/mol]	ν [cm^2/s]	ν [s^{-1}ML^{-1}] or [s^{-1}]*	Method
0.22	141	8.1×10^{-3}	1.8×10^{13}	Arrhenius plot
0.45	140	9.5×10^{-3}	1.6×10^{13}	heating rate variation
1.45	149 (β_2) 133 (β_1)	1.3×10^{-2} ---	2.1×10^{13} 6.1×10^{13}*	heating rate variation

Table 6.1: Desorption activation energies and frequency factors of chemisorbed oxygen on Au(110)-(1×2). The second-order frequency factor has the unit [cm^2/s], if related to absolute coverages (in [cm^{-2}]), and [s^{-1}ML^{-1}], if related to relative coverages (in [ML]). The first-order frequency factor of β_1 has the unit [s^{-1}] (*).

A closer inspection of the β_1 peak in Fig. 6.6 reveals a significant peak broadening with increasing heating rate (in contrast to β_2, which retains a constant width). This observation is consistent with the assumption that the β_1 state is due to the desorption of gold

oxide aggregates. The existence of aggregates leads to the exclusion of a certain fraction of the total coverage from the desorption process, viz., the O atoms inside the aggregates, because desorption is only possible from their edges or surfaces. That means, the total rate is lower than predicted by (or *inhibited* with respect to) a Polanyi-Wigner equation that depends on the *total* coverage. As a result, desorption will, with growing heating rate, extend over an increasing temperature range[2]. Alternatively, the β_1 peak could stem from the diffusion-controlled desorption of a surface-near bulk oxygen species. If the bulk diffusion is the rate-limiting step of the TD experiment, then we expect a peak broadening with increasing heating rate if the oxygen atoms have to diffuse over a range of different distances. However, the presence of a bulk species is unlikely because of the high reactivity of β_1 towards CO, as discussed in Chapter 11.

The results of our TDS analysis differ substantially from previous reports, especially with regard to the desorption order n. Atomic oxygen on Au(110)-(1×2), as studied by Sault et al. [Sa86], desorbed around 590 K (at a heating rate of 15 K/s) following a second-order kinetics at very low initial coverages ($\Theta_0 < 0.06$ ML). At higher coverages ($\Theta_0 >$ 0.25 ML), a change to first-order kinetics was observed. For $\Theta_0 = 0.5$ ML, the first-order frequency factor and desorption energy were found to be 1.3×10^{12} s^{-1} and 132 kJ/mol, respectively. Parker and Koel [Pa90] as well as Saliba et al. [Sa98] oxidized a Au(111) surface by exposure to ozone and obtained up to 1.2 ML of chemisorbed atomic oxygen. In contrast to our observations, the desorption followed a first-order kinetics over the *entire* coverage range. Low-coverage TD spectra (taken with a heating rate of 8.5 K/s) showed a desorption maximum around 520 K. With increasing coverages, the maximum shifted to higher temperatures and remained at 550 K for $\Theta_0 > 0.22$ ML. A frequency factor of 2.2×10^{11} s^{-1} and a desorption energy of 120 kJ/mol were reported.

6.2. Simulation of the thermal desorption spectra and kinetic modelling

6.2.1. Empirical approach

Interactions between adsorbate particles clearly influence the shape of the TD spectra and have to be considered in the analysis. In the Polanyi-Wigner equation (Eq. 4.1), these interactions were neglected by assuming a coverage-independent desorption energy. An empirical equation taking a correction to the desorption energy into account that depends linearly on the coverage is the so-called Elovich equation. This equation has been used extensively in the literature and is regarded as a good approximation especially for disordered adlayers (as in the present case) [Ma96]. Here, we employed a modified Elovich equation with an empirical correction, $E_{int}(\Theta)$, added to the desorption energy, E_{des}:

[2] See Section 10.1 for an extensive discussion of the exclusion effect.

$$R_{des} = \nu_n \Theta^n \exp\left(-\frac{E_{des} + E_{int}(\Theta)}{RT}\right) \qquad \text{(Eq. 6.1)}$$

The parameters E_{des}, ν_n, and n are assumed to be independent of coverage.

A numerical integration of Eq. 6.1 was carried out in order to simulate the TD spectra displayed in Fig. 6.1 for coverages up to 1 ML. For the simulation, we used an empirical energy correction given by $E_{int} = 15.8\ \text{kJ/mol} \times (\Theta - 0.25\ \text{ML})^{1.3}$ for $\Theta \geq 0.25$ ML and $E_{int} = 0$ for $\Theta < 0.25$ ML. A plot of $E_{int}(\Theta)$ is displayed in Fig. 6.8a. We emphasize that these relations for E_{int} are purely empirical, although they might possess some physical relevance. For example, in the case of a square array of equidistant O atoms, no next neighbour interactions can occur for $\Theta \leq 0.25$ ML. Accordingly, E_{int} should indeed vanish in this coverage range.

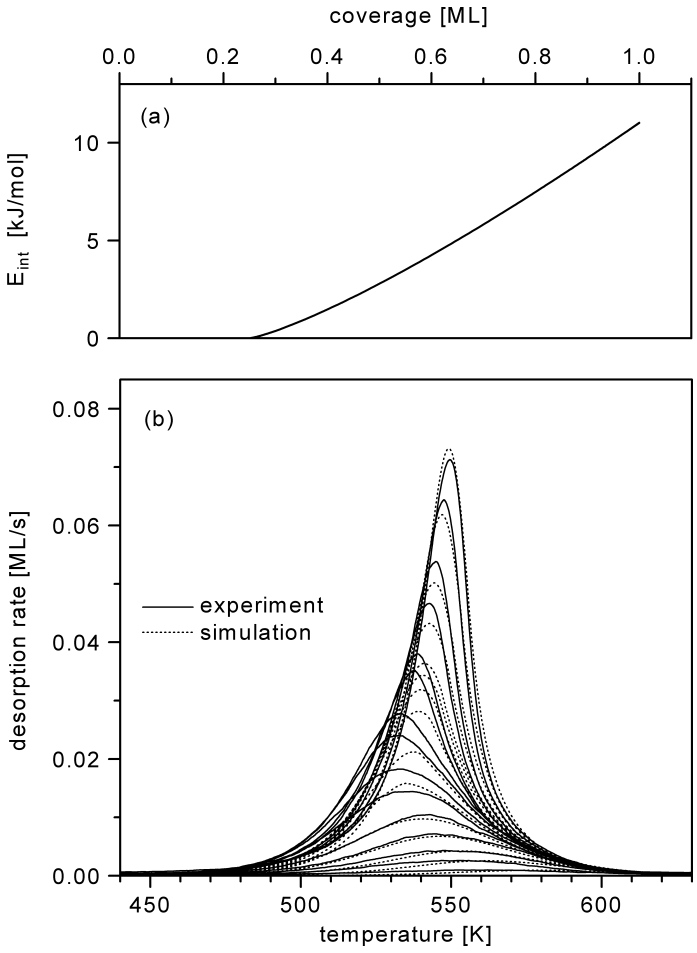

Fig. 6.8: Simulation of the TD spectra in Fig. 6.1 by numerical integration of Eq. 6.1. (a) Empirical correction to the desorption energy, $E_{int}(\Theta)$. (b) Experimental (solid lines) and simulated (dotted lines) TDS for coverages up to 1.0 ML. See text for the details.

The energy correction depends on the oxygen coverage with an exponent of 1.3. This deviation from the Elovich equation (which assumes $E_{int} \propto \Theta^{1.0}$) may reflect the fact that the frequency factor, which was constant in the simulation, depends actually on coverage. For the other parameters, we applied the values obtained by analysing the low-coverage TD spectra: E_{des} = 140 kJ/mol, $\nu_2 = 9.5\times10^{-3}$ cm^2s^{-1}, and n = 2. In Fig. 6.8b, we compare simulated and experimental spectra and find a remarkable agreement. We conclude that the spectra can be empirically simulated if we assume increasing attractive interactions between the oxygen atoms above 0.25 ML. However, the physical background of the energy curve in Fig. 6.8a remains speculative, and the assumption of a constant frequency factor is not necessarily a reasonable approximation. Finally, the underlying mechanism may be more complex, as discussed in the following subsection.

6.2.2. Two-phase model of the desorption kinetics

A quantitative *and* qualitative understanding of the desorption kinetics is provided by a model based on the formation of oxygen islands and the existence of a two-dimensional phase equilibrium during desorption[3]. There are various indications for an island formation, especially the coverage dependence of the CO oxidation rate and the work function change with temperature (see Sections 6.5, 6.6 and Section 11.2). Furthermore, the unperturbed second-order kinetics at low coverages suggests an adsorbate phase in which the oxygen atoms are fairly mobile at the desorption temperature. We may therefore assume that both islands and a mobile phase exist on the surface during desorption; and we propose that the desorption process is accompanied by a phase equilibrium between oxygen islands as a two-dimensional condensed (tc in abbreviation) phase on the one hand and a two-dimensional gas (tg) phase on the other. Desorption may occur from both phases, but with different local rates, R_{tc} and R_{tg}. R_{tc} is smaller than R_{tg}, reflecting the attractive interactions between the oxygen atoms in the islands. We further assume that the local coverages of both tc and tg-phase are constant as long as the phase equilibrium is established, i.e., we neglect the temperature-dependence of the equilibrium constant (see below).

What are the consequences of the different local rates? At high coverages, the surface is predominantly covered with O islands (tc-phase) possessing a low local desorption rate. The overall (total) rate, R_{tot}, is therefore small; and the desorption appears to be inhibited. As desorption proceeds, the islands shrink, giving way for the tg-phase with the higher local rate R_{tg}. As a result, the desorption process accelerates autocatalytically *in addition* to the effect of the temperature increase. The isothermal desorption rate, $R_{des}(\Theta)_T$, as displayed in Fig. 6.2, increases despite decreasing coverage.

[3] See Section 4.1.4 for a general discussion of desorption in the presence of a two-dimensional phase equilibrium.

As soon as the tc-phase has vanished, desorption occurs from a uniform tg-phase, and the system returns to ordinary second-order kinetics. At this point, the total coverage, Θ_{tot}, equals the local coverage of the tg-phase during the phase equilibrium. Therefore, we can regard the coverage at which desorption begins to deviate from second order as the local coverage of the tg-phase in equilibrium. According to Section 6.1.2, this coverage is $\Theta_{tg}^{crit} = 0.35$ ML. For the local coverage of the tc-phase we assume $\Theta_{tc}^{crit} = 1.0$ ML, since no further significant changes occur in the TDS coverage series in Fig. 6.1 between 0.35 and 1.0 ML.

The kinetic model was formalized as outlined in Section 4.1.4: The total desorption rate, R_{tot}, is given by the sum of the local rates, R_{tc} and R_{tg}, weighted with the surface fractions, F_{tc} and F_{tg}, of the respective phases:

$$R_{tot} \equiv -\frac{d\Theta_{tot}}{dt} = R_{tc} F_{tc} + R_{tg} F_{tg} \quad . \qquad \text{(Eq. 6.2)}$$

For calculating the local rates we apply the second-order Polanyi-Wigner equation:

$$R_i = \nu_i \Theta_i^2 \exp\left(-\frac{E_{des}(i)}{RT}\right) \qquad \text{(Eq. 6.3)}$$

with $i \in \{tg,tc\}$.

The fraction of the surface, F_{tc}, which is occupied by the tc-phase, i.e., the ratio of the surface area covered by islands, A_{tc}, and the total surface area, A_{tot}, is given by:

$$F_{tc} \equiv \frac{A_{tc}}{A_{tot}} = \frac{\Theta_{tot} - \Theta_{tg}^{crit}}{\Theta_{tc} - \Theta_{tg}^{crit}} \qquad \text{(Eq. 6.4)}$$

(with the local coverages $\Theta_{tc}^{crit} = 1.0$ ML and $\Theta_{tg}^{crit} = 0.35$ ML) for $\Theta_{tot} > \Theta_{tg}^{crit}$; and $F_{tc} = 0$ else.

Obviously, the surface fraction of the tg-phase is $F_{tg} = 1 - F_{tc}$.

Finally, the total coverage can be calculated by Eq. 6.5:

$$\Theta_{tot}(t) = \Theta_0 - \int_0^t R_{tot}\, dt' \quad . \qquad \text{(Eq. 6.5)}$$

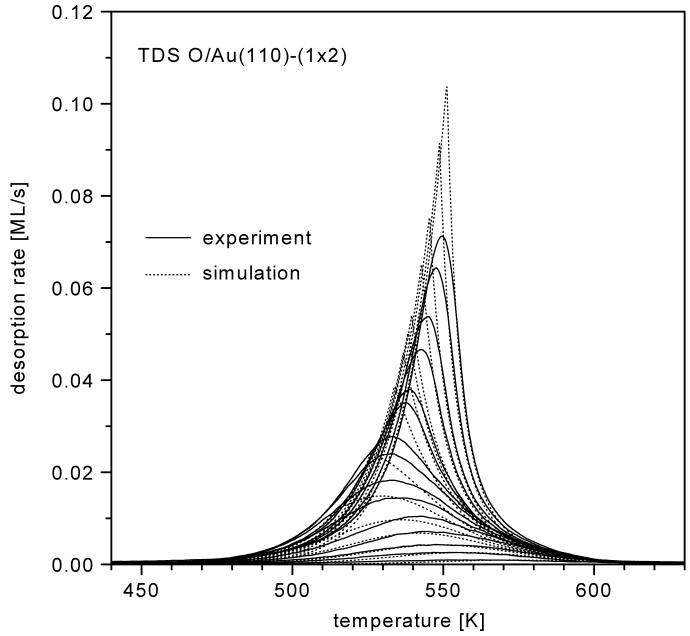

Fig. 6.9: Simulation of the TD spectra in Fig. 6.1 by numerical integration of Eqs. 6.2-6.5. Experimental (solid lines) and simulated (dotted lines) TDS for coverages up to 1.0 ML. The parameters employed for the simulation are $E_{des}(tg) = 140$ kJ/mol, $\nu_2(tg) = 9.5\times10^{-3}$ cm^{2}s^{-1}, $E_{des}(tc) = 151$ kJ/mol, $\nu_2(tc) = 6.8\times10^{-3}$ cm^{2}s^{-1}, $\Theta_{tc}^{crit} = 1.0$ ML, and $\Theta_{tg}^{crit} = 0.35$ ML. The spectra correspond to the following initial coverages (in ML): 0.04; 0.09; 0.14; 0.22; 0.31; 0.43; 0.52; 0.62; 0.66; 0.69; 0.71; 0.78; 0.84; 0.93; 1.00.

As an example, we applied the activation parameters obtained from the HRV at $\Theta_0 = 0.45$ ML ($\Theta_{max} = 0.23$ ML, see Tab. 6.1) were applied for calculating R_{tg}. We deliberately avoided to determine these parameters by a fit of the whole range of the experimental spectra, since we considered it more important to demonstrate that the desorption process is mainly controlled by the desorption from the tg-phase, which has to compete with the islands (tc-phase) for the surface area. Accordingly, we used the desorption activation parameters for the low-coverage range as extracted from the experimental data in Section 6.1.2.

In order to find appropriate desorption parameters for the tc-phase, which are not experimentally accessible, we employed transition state theory [Ey35, Gl41, Ey44]. Assuming a completely immobile adsorbate for this phase, we obtained a frequency factor of $\nu_2(tc) = 1.15\times10^{13}$ s^{-1}ML^{-1} or 6.8×10^{-3} cm^{2}s^{-1} (see Appendix, Section 6.7). Finally, we were left with just one free parameter, viz., the desorption energy from the tc-phase, which was adjusted in the process of the numerical integration of Eq. 6.2. The best agreement between experimental and simulated spectra, as shown in Fig. 6.9, was achieved with a value of $E_{des}(tc) = 151$ kJ/mol. The difference $\Delta E_{des} = E_{des}(tc) - E_{des}(tg) = 11$ kJ/mol may be interpreted as the mean interaction energy of the oxygen atoms within the islands. However, this value depends on the choice of ν_2 and is therefore not particularly reliable. If we assume a partially immobile layer with only rotational

freedom for the activated complex, we obtain a frequency factor of $\nu_2(tc) = 1.32\times10^{14}\ s^{-1}ML^{-1}$ or $0.079\ cm^2s^{-1}$ (see Appendix, Section 6.7), and a significantly larger value of $\Delta E_{des} = 21$ kJ/mol results.

A complete agreement between experiment and simulation cannot be expected, since the chemisorbed oxygen does certainly not form a completely uniform adsorbate state, but rather a range of states with similar desorption energies, as LEED investigations, showing a completely disordered chemisorbed oxygen phase, suggest (see Section 6.3 and Refs. [Sa86], [Sa98]). Furthermore, different sizes and curvatures of the islands may lead to slightly different binding energies of the oxygen atoms, resulting in a general peak broadening. Introducing additional parameters, e.g., a coverage-dependent activation energy, led to an improved agreement, which, however, has no theoretical foundation. We therefore refrained from complicating our model in this way.

A similar desorption kinetics with unusual sharp TD peaks, shifting to higher temperatures above a certain coverage, was also observed for the desorption of high coverages of nitrogen on Cu(111) [Sk98] and for oxygen on Pd(111) [Kl01]. In both cases, the TD spectra were successfully simulated by similar two-phase models, which completely excluded desorption from the condensed phase. The fact of island formation was confirmed by STM measurements for both systems.

In the following paragraph, we add some further remarks concerning the assumption of a two-dimensional phase equilibrium: 1.) The local coverages of both two-dimensional phases were considered to be constant, although the temperature increase during the TDS experiment will influence the equilibrium constant, $K_\Theta = \Theta(tg)/\Theta(tc)$, and thereby increase the coverage of the tg-phase, $\Theta(tg)$. This point deserves attention, since, with the $\Delta E_{des} = 11$ kJ/mol as calculated above, K_Θ changes by a factor of approximately 1.15 between 520 K and 550 K. The autocatalytic behaviour could *partly* be due to this effect, because a higher $\Theta(tg)$ leads to an increased total desorption rate. The quantitative treatment of the shift of the equilibrium constant requires the exact knowledge of ΔE_{des}. Since our estimate of ΔE_{des} relies only on transition state theory, we refrained from explicitly considering this effect in the simulation[4].

2.) We restricted the two-dimensional phase equilibrium to *two phases*, a gas phase and a condensed phase, both in direct contact with the substrate. In similar discussions of two-dimensional phase equilibria during desorption processes often a three-phase system is considered with a two-dimensional gas phase *on* the islands ('second-layer gas', '2LG' in abbreviation) as the third phase (see, for example, [Ve76a, As82, As89]). This model was successfully applied mainly to rare gas and metal desorption, i.e., to systems with similar binding energies for first and second adsorbate layer. For a chemisorbed system the

[4] The approximate temperature-dependence of K_Θ is given by:

$$\frac{\partial \ln K_\Theta}{\partial T} \approx \frac{\Delta E_{des}}{RT^2}.$$

assumption of a 2LG appears rather artificial, since the binding energies of first-layer gas (1LG) and 2LG may differ by one order of magnitude or more. Accordingly, Asada and Masuda [As89] remarked that "our model cannot be applied to an adsorption system that does not form multilayers, e.g. ... O_2/Ag(110) ...". Nevertheless, the idea of a three-phase system has been generalized with the argument that the density of the 2LG may be very small (due to the large energy difference to the 1LG), but that the very weak bonding will ensure a substantial desorption rate. This rate is said to be equal to that of the 1LG for the same thermodynamical reason as mentioned in the next paragraph. Here we have to make the following objection: The rate-limiting step in the desorption from the 2LG may well be the transfer of a particle from the 1LG to the 2LG, rather than its desorption, especially in strongly bound chemisorbed systems. If this is the case, no equilibrium between 1LG and 2LG can be established, and we may neglect the possible existence of a 2LG phase, since it will not contribute to the total desorption rate. (Elementary reactions following the rate-limiting step and being significantly faster than this do not influence the overall rate.)

3.) It has been claimed that "zero-order desorption must generally be observed in any kind of phase equilibrium" [Na84, Na87] on the surface, an assumption that is still widely accepted. If this applies to our case, a phase equilibrium as assumed for our system would inevitably lead to a zero-order instead of the observed autocatalytic desorption. The assumption of a zero-order desorption is usually justified by a thermodynamical argument: As Lehner et al. [Le01] put it, "the chemical potential μ of the two coexisting phases is equal and, thus, also the desorption rate per unit area". The conclusion drawn herein, however, holds only if the sticking coefficients of both phases are equal, as emphasized by Payne and Kreuzer [Pa88a, Kr88]. In the case of our system, the sticking coefficient for dissociative oxygen adsorption is certainly lower on the islands (tc-phase) than on the tg-phase. Therefore, also the desorption rate from the islands is lower, in accordance with our observations.

6.2.3. ‘Explosive desorption’ and other models

A) A narrow TD peak shape has often been observed for surface reactions as, for example, the decomposition of carboxylate and formiate (see [Sh95] and references therein). For explaining this phenomenon, frequently referred to as ‘surface explosion’ or ‘explosive desorption’, two models have been proposed: second-order autocatalysis and the circular island model. The former model assumes that the yield is proportional to both the density of the adsorbed species and the density of empty sites. Therefore, it is only appropriate for *dissociative* desorption of an adsorbate that is arranged randomly on the surface and needs no further consideration in our context. In contrast, the circular island model assumes island formation and may be of physical relevance to our system. In this model, desorption initiates at specific sites on the surface and then proceeds along the circumference of circles of increasing radius centred on these initiation sites. However,

this model in its original form as proposed by Falconer and Madix [Fa74] provides rather poor fits, whereas the more sophisticated form by Sharpe and Bowker [Sh95] demands the knowledge of a number of microscopic parameters, which are not available for our system. Therefore, we did not further pursue this approach.

B) The Bethe-Peierls approximation (BPA) [Be35, Pe36] is a convenient method to deal with adsorbate interactions. The results concerning thermal desorption are usually in good agreement with numerical solutions as obtained by Monte-Carlo simulation, at least for not too high interaction energies ($E_{int}/RT < 1.35$). Here, we considered a completely mobile adsorbate layer and followed the treatment given by Masel [Ma96]. We attempted to fit the low-coverage range of the spectra in Fig. 6.1 using Eq. 6.6:

$$R_{des} = \nu_2 \exp\left(-\frac{E_{des} + E_{corr}}{RT}\right)\Theta^2 \frac{\exp(E_{int}/RT)}{1+\Theta\exp(E_{int}/RT)} \qquad \text{(Eq. 6.6)}$$

assuming (a) a coverage-independent ($E_{corr} = 0$) and (b) a coverage-dependent rate constant ($E_{corr} = f(\Theta)$). With assumption (a), neither the second-order kinetics at low coverages nor the over-crossing of the leading edges was reproduced. Assuming $E_{corr} = f(\Theta) \propto \Theta$ (case b), we found that the second-order kinetics at low coverages was not reproduced. This could only be achieved with an empirical function $E_{corr} = E_{int}(\Theta)$ similar to that used in section 6.2.1., but even then a poorer fit than with Eq. 6.1 alone was obtained.

We conclude that the two-phase model employed in Section 6.2.2 is apparently the most appropriate among those of physical relevance to our system. It requires a minimum set of parameters, which are directly available from experimental data (with one exception), and leads to a sufficient agreement between experimental and simulated spectra. The empirical model as described in Section 6.2.1 provides actually an even better numerical agreement with the experiment, but the physical relevance of the coverage-dependent interaction energy E_{int} (as displayed in Fig. 6.8a) remains completely unclear. Presently, no reliable discrimination between both models is possible on grounds of the experimental data. A real-time STM investigation of the desorption process (which is unfortunately still far from being a routine measurement) could probably clarify this point.

6.3. Low-energy electron diffraction (LEED)

LEED patterns obtained at 300 K for increasing coverages of chemisorbed oxygen are displayed in Fig. 6.10. The clean surface is known to reconstruct in a 'missing-row' structure, responsible for the characteristic (1×2) pattern in Fig. 6.10A. Oxygen chemisorption causes an increasing suppression of the substrate spots and an enhanced back-

ground intensity, as shown in Figs. 6.10B and 6.10C for coverages of 0.25 ML and 0.5 ML chemisorbed oxygen, respectively, taken after 3 minutes of electron bombardment (500 eV, 3.9 μA/cm^2) of 3.8 L (7.5 L) O_2. A complete suppression of the substrate lattice spots occurred above 0.9 ML (Fig. 6.10D). The lack of any additional reflexes due to the adsorbate and the disappearance of the substrate spots both indicate a general loss of long-range order within the substrate surface region and, hence, a significant displacement of the gold surface atoms. Regaining an ordered substrate structure (or obtaining an ordered adsorbate structure) by prolonged annealing close to the oxygen desorption temperature (420 K) for up to one hour proved unsuccessful. Re-establishing substrate long-range order is only possible through the complete removal of the chemisorbed oxygen by thermal desorption, sputtering, or reaction with carbon monoxide.

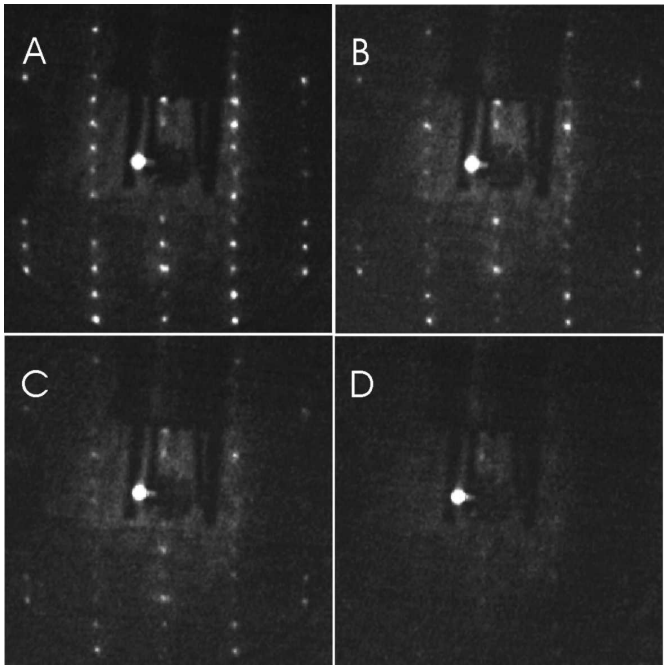

Fig. 6.10. LEED patterns of chemisorbed oxygen on Au(110)-(1×2). The photographs were taken at 300 K using an incident beam energy of 260 eV. Oxygen chemisorption causes an increasing suppression of the substrate spots and an enhanced background intensity: (A) Clean Au(110)-(1×2) surface, (B) 0.25 ML, (C) 0.5 ML, (D) 0.9 ML chemisorbed oxygen. The large spot close to the centre is an artefact arising from reflection from the sample holder.

These LEED results resemble those reported for oxygen on Au(110)-(1×2) [Sa86] and Au(111) [Sa98], in which oxygen atoms were produced by thermal pre-dissociation and decomposition of ozone on the surface, respectively. In both cases, a large increase in background intensity due to a disruption of the long-range order of the substrate was observed, but no ordered overlayer patterns at any coverage or annealing temperature were seen.

The reluctance of chemisorbed oxygen to form ordered adlayers on gold surfaces, together with the destruction of the substrate lattice, might be related to the properties and especially to the complicated crystal structure of bulk gold(III) oxide, Au_2O_3 [Jo79]. For this argument, we consider the oxygen-gold bond in the oxide as a prototype for the respective chemisorptive bond. Au_2O_3 possesses a very large unit cell containing a complicated network structure of corner-linked distorted square-planar [AuO_4]-units and is quite different from a typical ionic crystal, which has a small, highly symmetric unit cell. These peculiarities indicate significant directional (and therefore covalent) contributions to the Au-O bond. Since covalent bonds demand a certain coordination geometry, formation of the Au-O bonds on the surface may cause the displacement of gold atoms. Such a displacement requires far less energy than the distortion of a covalent bond, since the metallic bond is much less directional than its covalent counterpart.

6.4. UV photoelectron spectroscopy (UPS)

In this section, we report on photoemission spectra of adsorbed *atomic* oxygen rather than *molecular* oxygen, which was studied in Chapter 5 (see also [Go02]). Fig. 6.11 shows a series of UV photoelectron spectra ($h\nu = 24$ eV) measured after warming the chemisorbed oxygen phase with an initial coverage of $\Theta_0 = 1.75$ ML to the indicated temperatures[5]. The UP spectrum of the clean gold surface (bold line) is characterized by a sharp, but low, Fermi edge and by an intense d-band structure between ≈2 and 8 eV below the Fermi level (E_F). The chemisorption of oxygen atoms on this surface causes then an additional photoelectron emission between E_F and 2.0 eV below E_F, which is clearly visible in the original UP spectra (see, for example, the spectrum corresponding to 300 K). Further oxygen-induced emissions overlap with the gold d-band signals so that the effect of chemisorption can more clearly be seen in the difference spectrum, which corresponds to the initial coverage of 1.75 ML. The difference spectrum reveals additional emissions around 2.6 eV and 5.0 eV below E_F. The sharp minima at 2.2 eV and 3.2 eV below E_F are due to a strong attenuation of the respective Au 5d signals caused by the oxygen adsorption. We observed the same attenuation also during adsorption of other gases, e.g., O_2 (Section 5.1.2 and [Go02]), CO (Section 8.2 and [Go03]), CO_2 (Section 10.2), as well as Ar and Kr [Sc03], i.e., even in the case of pure physisorption. Presumably, these variations in the Au 5d-band intensity are caused by scattering of the photoexcited d-electrons on the adsorbed particles (see Ref. [Ja83]) and/or to some disordering at the surface (al-

[5] In our temperature-dependent UP and $\Delta\varphi$ measurements (as described in Section 6.5), the heating current had to be switched off during the spectra recording in order to avoid perturbations caused by the magnetic field and the electric potential on the sample. As a result, the sample temperature decreased by ≈ 15 K over the measurement time of 20 seconds in the case of UPS, or by ≈ 5 K in the case of $\Delta\varphi$. These deviations are tolerable since the UP spectra and the work function change predominantly depend on the adsorbate coverage, which is controlled by the desorption rate, R_{des}. R_{des} depends exponentially on temperature and, therefore, only the indicated *maximum* temperatures are important.

though the latter could not be observed at least in the case of rare gas adsorption)[6]. It appears impossible to disentangle the features occuring between ≈2.0 and ≈4.0 eV below E_F and to ascribe them to oxygen-induced states. However, it is likely that chemisorbed oxygen also contributes to the photoemission signal in this region. An indication is the peak at 2.6 eV in the difference spectrum, where the oxygen-induced emission is obviously *not* overcompensated by the attenuation of the Au 5d signal.

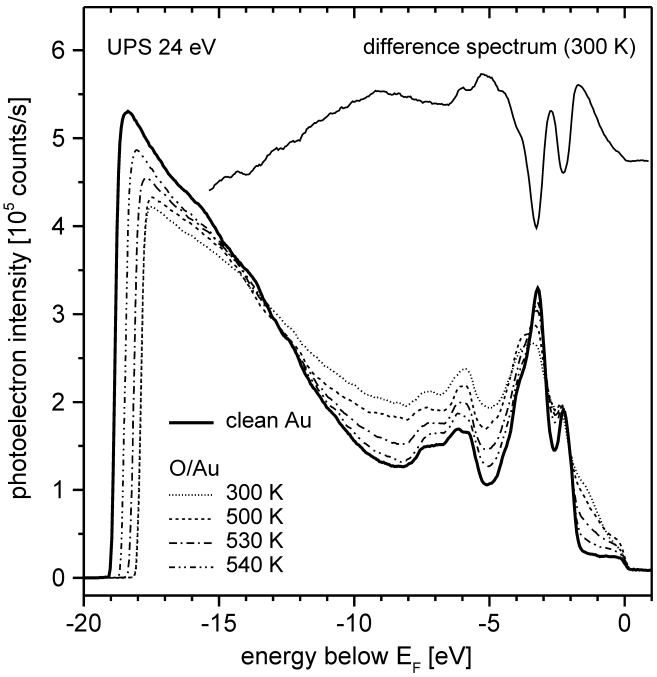

Fig. 6.11: UV photoelectron spectra of chemisorbed oxygen on Au(110)-(1×2) at various temperatures. The 300 K spectrum and the difference spectrum correspond to an oxygen coverage of 1.75 ML. The bold solid line represents the spectrum of the clean Au surface. The UV radiation (hν = 24 eV) had an incidence angle of $\vartheta_i = 45°$ (polar) and $\phi_i = 0°$ (azimuthal) and was p polarized with respect to the $(00\bar{1})$ plane (cf. Section 4.2). The ejected electrons were detected normal to the surface ($\phi = 0°$). For the further experimental details see Section 4.2.

According to Section 6.1, two oxygen species β_1 (gold oxide) and β_2 (chemisorbed atomic oxygen) exist on the gold surface at 300 K, if the initial coverage exceeds 1.0 ML. Both oxygen species, although clearly distinguishable in TDS, lead to the same features in UPS. This is evident from Fig. 6.11 as well as from an UPS series for increasing coverages as displayed in Fig. 6.12. Heating to 500 K leads to the complete desorption of β_1 (but not of β_2) and thereby, for $\Theta_0 = 1.75$ ML, to the loss of 40% of the initial oxygen coverage[7]. However, Fig. 6.11 shows almost no change in position or intensity of the

[6] It should be mentioned that a similar general attenuation effect of adsorption on the d-band emission has been reported for Ag(110) [Tj90].

[7] The coverage as a function of temperature for several initial oxygen coverages Θ_0 is displayed in Fig. 6.14b.

photoelectron signals. Only the desorption of β_2 between 500 K and 600 K is accompanied by a reduction of the oxygen-induced emissions, an effect which is most obvious for the signal between 0 and 2.0 eV below E_F.

Comparison with literature data is not particularly productive since chemisorption of oxygen on gold surfaces has not been studied by valence level photoelectron spectroscopy prior to this work. There are, however, few reports concerning gold oxide or oxyhydroxide. Peuckert et al. [Pe84] produced thick layers of AuOOH on Au(100) by electrochemical oxidation and found a broad peak ranging from 1 eV to 10 eV with a maximum at 5.5 eV in the valence band region of the Mg-K_α induced XP spectrum. Mg-K_α radiation was also used by Aita and Tran [Ai91] for investigating Au/Au-oxide cermet films (thickness 70 nm), produced by reactive sputter deposition. The XP spectra reported by these authors exhibit broad emission features between E_F and 10 eV below E_F with maxima at 3.7 eV and 5.9 eV. A relation between these XPS reports and UV valence level spectroscopy was established by Koslowski et al. [Ko01]. The authors used both Al-K_α and He-II radiation in order to probe a 3.3 nm gold oxide film produced by oxidation of a gold film with preferential (111)-orientation in an oxygen plasma. In the case of excitation by x-rays, the difference spectrum of the valence band range showed additional oxygen-induced intensity around 1.7, 3.3, 5.2, and 8.5 eV below E_F. In the He-II UP spectrum, similar but much broader peaks appeared. Clearly, the comparison with previous reports reveals that the UP spectrum of gold oxide closely resembles our UP spectra of chemisorbed oxygen. Accordingly, the formation of gold oxide (β_1 state) on the oxygen-covered surface (β_2 state) did not significantly alter our UP spectra.

Alternatively, one may argue that coverages above 1.0 ML cause no significant changes in the UP spectrum because the β_1 oxygen species does not contribute to emissions in the valence band range. We consider two possible reasons that may lead to this behaviour: (i) the β_1 oxygen does not contribute any emission intensity in this energy range at all, and (ii) this oxygen species is located deeper in the crystal (forming subsurface or bulk oxygen) than the inelastic mean free path λ_{imfp} of the photoelectrons (λ_{imfp} is ≈ 4 atomic layers around 20 eV electron energy). Reason (i) appears highly unlikely, and (ii) can be safely excluded, since β_1 oxygen reacts eagerly with CO from the gas phase (see Chapter 11), i.e., it is definitely located *on* the surface.

Since thermal desorption spectroscopy is a 'destructive' method, which may also induce thermally activated surface processes within an adsorbate layer, the question arises whether desorption states, measured at elevated temperatures and under kinetic control, actually reflect the equilibrium state of the adsorbate. Significant temperature-induced adsorbate changes may prevent a correct interpretation of the TDS data. It is therefore necessary to continuously monitor the UP spectra during the gradual thermal desorption of the adsorbate (Fig. 6.11) and to compare them with the spectra measured at room temperature for different coverages. These spectra, taken directly after preparation of the respective oxygen phases, are displayed in Fig. 6.12 and closely resemble those shown in

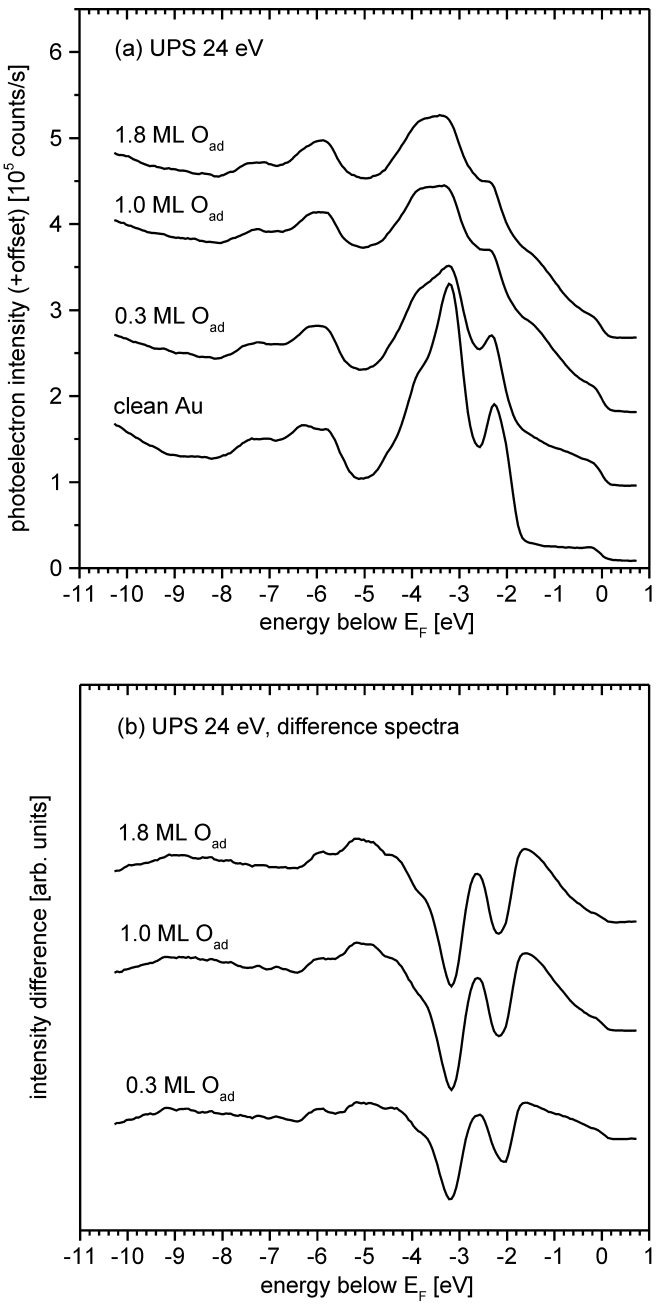

Fig. 6.12: UV photoelectron spectra of clean and oxygen-covered Au(110)-(1×2): (a) original spectra and (b) difference spectra. Oxygen coverages as indicated. The spectra were measured at 300 K in normal emission with a photon energy of 24 eV. The experimental details are described in Section 4.2.

Fig. 6.11. There is no evidence delivered by UPS that our conclusions drawn from TDS are not applicable also to the adsorbate state below desorption temperature.

In our angle-resolved photoemission (ARUPS) experiments, none of the peaks showed any dispersion with parallel or perpendicular momentum. Using linearly polarized radiation, variation of the beam incidence angle had no influence on the relative peak intensi-

ties. Both observations suggest a disordered oxygen adsorbate phase, in accordance with previous LEED findings (see Section 6.3 and [Sa86], [Sa98]).

The oxygen-induced emission close to E_F resembles partly that found for the analogous copper and silver systems: In the case of Ag(110)-p(2x1)O, signals between 1.5 eV and 3.0 eV below E_F (here strongly dispersive) were found and attributed to anti-bonding bands of the O(2p)-Ag(4d) interaction [Tj90]. Additionally, emissions in the range between 4.0 eV and 6.5 eV were observed (see [Co97] and references therein). The oxygen-induced surface states on Cu(110)-p(2x1)O are characterized by three bonding bands in the energy range between 7.8 eV and 5.4 eV below E_F, accompanied by occupied anti-bonding states between 1.2 eV and 2.0 eV below E_F (see again [Co97] and references therein).

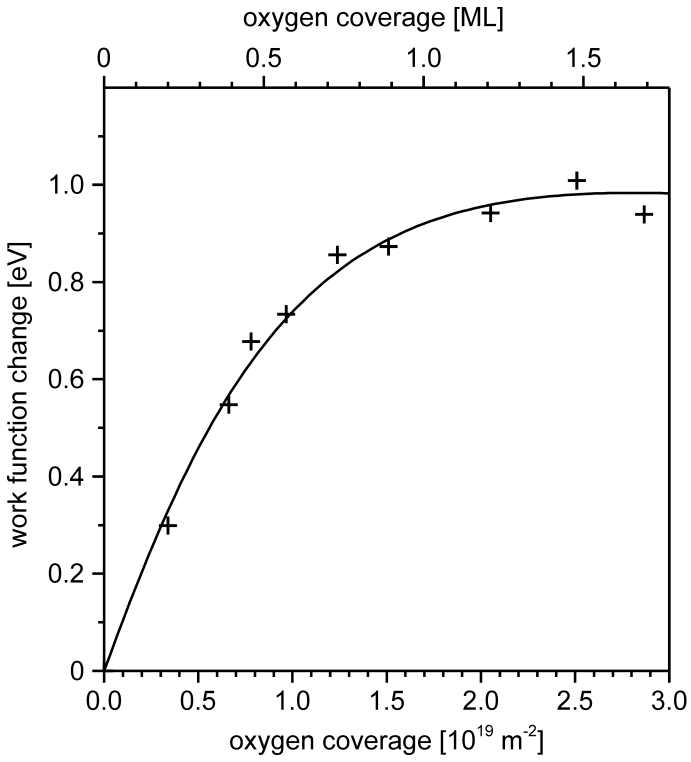

Fig. 6.13: Oxygen-induced work function change as a function of the initial O coverage at 300 K. The solid line is a fit using Eq. 4.49 with $\mu_0 = 0.27$ D and $\alpha = 1.5\times10^{-24}$ cm^3.

6.5. Work function measurements (Δφ)

Fig. 6.13 displays the work function change as a function of oxygen coverage (as determined by TDS) at 300 K. The different O coverages were obtained by varying the initial coverages of physisorbed molecular oxygen. Obviously, oxygen chemisorption causes a work function increase, which indicates a charge transfer from gold to oxygen. For the further analysis of the $\Delta\varphi(\Theta)$ curve we employed the well-known Topping formula

(Eq. 4.49) [To27]. In Fig. 6.13, the solid curve is a data fit using Eq. 4.49 with μ_0 = 0.27 D and $\alpha = 1.5\times10^{-24}$ cm^3. Thus, the polarizability equals that of free oxygen atoms, $(1.5\pm0.5)\times10^{-24}$ cm^3 [An70]. The initial dipole moment allows the estimation of the formal charge separation and, therefore, of the ionicity of the O-Au bond, if the O-Au distance is known. In solid Au_2O_3, four different O-Au distances between 1.93 Å and 2.07 Å were determined [Jo79]. Using the mean value of 2.0 Å, we obtain a formal charge separation of 0.021 e_0, which is similar to that in carbon monoxide (0.022 e_0), but much smaller than that of bonds with strong ionic contributions as HCl (0.18 e_0). Thus, the chemisorptive O-Au bond is obviously rather covalent with only minor ionic contributions. This result is consistent with Pauling's electronegativity scale, on which Au has the highest value of all metals (2.54), close to that of carbon (2.55) [Al61], whereas oxygen has a Pauling electronegativity of 3.44 (cf. Tables 2.1 and 2.3). We note that only the perpendicular component of the dipole moment contributes to the work function change. As a consequence, the actual charge separation may be higher than the calculated value, if the orientation of the O-Au bond is not normal to the surface. Additionally, the oxygen-covered surface is disordered and may contain O atoms in different vertical positions, which can lead to a partial cancellation of the individual contributions to $\Delta\varphi$. For these reasons, the calculated charge separation has to be regarded as a lower limit of the true value, and the O-Au bond might be more ionic than stated above. However, support for a covalent model of the surface O-Au bond is also delivered by the work of Koslowski et al. [Ko01]. These authors investigated Au_2O_3 by XPS and UPS and found evidence for a strong hybridization between Au 5d and O 2p orbitals, which suggests significant covalent contributions to the O-Au bond.

Comparison with literature data shows that our results resemble those for O/Au(111) as reported by Saliba et al. [Sa98]. In that work, the coverage dependence of the oxygen-induced work function change was also well described by the Topping equation. The higher values for the initial dipole moment, μ_0 = 0.34 D, and the polarizability, $\alpha = 2.4\times10^{-24}$ cm^3, may partly be due to the different method for determining the oxygen surface concentration.

Due to the temperature-dependence of the oxygen coverage, also the O-induced work function change depends on the temperature and on the thermal treatment of the O-covered sample, as it will be illustrated in the following paragraph. In Fig. 6.14a, $\Delta\varphi$ is plotted vs. temperature for several initial oxygen coverages ranging fom 0.20 ML to 1.48 ML. The temperature-dependence of the corresponding oxygen coverages, obtained by integration of thermal desorption spectra, is plotted in Fig. 6.14b. The same *initial* coverages were applied in the Figs. 6.14a and 6.14b. Generally, a substantial work function reduction of up to 1.0 eV is observed for T > 500 K. As seen from Fig. 6.14b, this change is caused by the desorption of the β_2 state. In the temperature range between 300 K and 500 K, changes in φ remain small, especially for low initial coverages (0.20 ML and 0.39 ML).

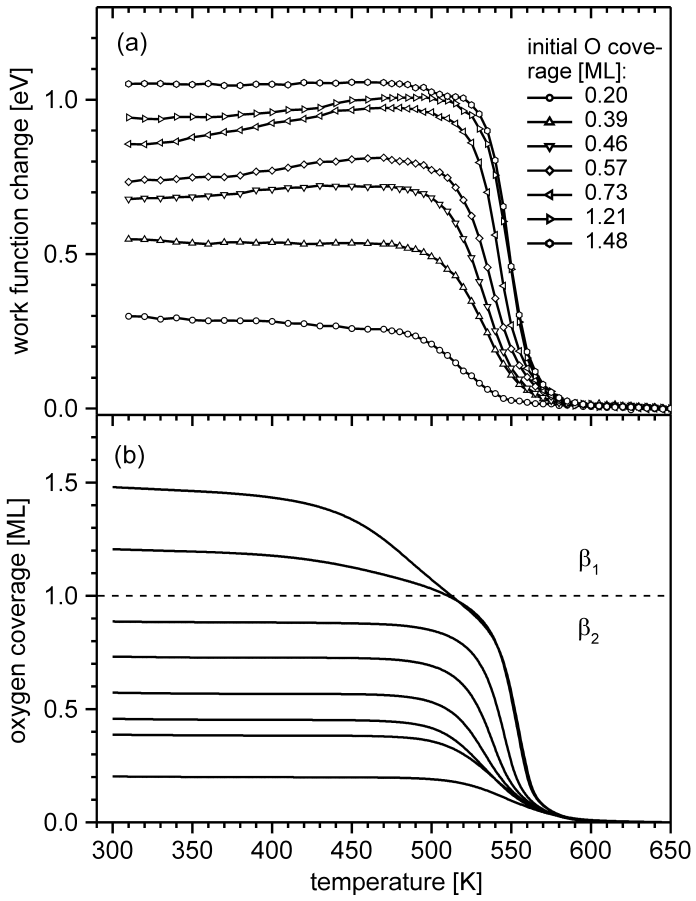

Fig. 6.14: (a) Oxygen-induced work function change as a function of temperature for several initial O coverages. (b) Oxygen coverage as a function of temperature. Each Θ(T) curve in (b) corresponds precisely to a Δφ(T) curve in (a).

However, for Θ_0 = 0.46 ML, 0.57 ML, and 0.73 ML, a significant work function increase is observed. In this coverage range, TDS (Section 6.1) and RTDM (i.e., CO oxidation, see Chapter 11) experiments suggest the existence of oxygen island on the surface, and the work function data support this interpretation, as discussed in Section 6.6. For initial coverages above one monolayer, no work function reduction occurs between 300 K and 500 K, despite the significant loss in coverage due to the desorption of β_1 beyond 400 K. Therefore, the β_1 state should not correspond to chemisorbed oxygen atoms on the surface, and neither to subsurface oxygen, which generally lowers the work function. More likely, a three-dimensional gold oxide species with a similar (or lower) work function as an oxygen monolayer may exist on the gold surface. The possible assignment of β_1 to a bulk oxygen species, which should also not influence the surface potential, is excluded by its high reactivity towards CO.

6.6. Discussion

In Section 6.1, we considered the thermal desorption behaviour of chemisorbed oxygen on the gold (110)-(1×2) surface. We found that the desorption process is controlled by a complex kinetics, and we suggested two different models for the simulation of the TD spectra. One of these models based on the assumption of a strongly coverage-dependent desorption activation energy (model 1), while the other model postulated the existence of a phase equilibrium between islands (as a two-dimensional condensed phase) and a two-dimensional gas phase on the surface (model 2). Although model 1 provided a better fit of the experimental data, we favoured model 2, because it requires only a minimum set of assumptions and appears to be less arbitrary. With respect to the adsorbate structure, the models differ in one important point: model 1 inherently assumes a uniform oxygen phase, while the two-phase model essentially bases on the existence of islands (or other aggregates) of oxygen atoms. In the preceding sections of this chapter, we presented data which support the two-phase model of the desorption process by suggesting that oxygen islands indeed exist on the gold surface. The following discussion will mainly focus on this point.

The RTDM curves displayed in Fig. 11.2 show that the reaction rate depends not only on the *instantaneous* oxygen coverage (as expected for an uniform oxygen phase), but also on the *initial* coverage. A similar behaviour has previously been observed by Outka and Madix [Ou86] in the case of chemisorbed oxygen on Au(110)-(1×2), obtained by thermal dissociation of O_2 on a hot Pt wire close to the surface. The dependence of the reaction rate on the initial coverage was qualitatively attributed to the presence of clusters or islands of oxygen atoms. These aggregates react preferably at their perimeter with the smaller islands being the most reactive. Therefore, high oxygen coverages lead to a small initial rate since the oxygen is predominantly contained in large islands which react slowly.

A further support for the two-phase model is delivered by the temperature dependence of the oxygen-induced work function change. For medium initial coverages (i.e., for Θ_0 = 0.46 ML, 0.57 ML, and 0.73 ML), a significant work function increase was observed in the temperature range between 300 K and 500 K, although, according to TDS, no oxygen desorption occurred in this range. This result again suggests the existence of island of oxygen atoms, in which the small O-O distance leads to a mutual depolarization of the individual oxygen-gold complexes. Raising the temperature may cause a partial dissolution of these islands. The increasing mean distance between the O atoms reduces the amount of depolarization, and the contribution of each adsorbate-substrate complex to the total work function change grows. This eventually causes the observed work function increase. In full agreement with this interpretation, no work function reduction occurred between 300 K and 500 K, if the initial coverage exceeded one monolayer. In this case, no vacant adsorption sites are available for island dissolution. Reversely, no work function increase was observed in this temperature range for low initial coverages, because

the formation of island requires a certain critical coverage. In our thermal desorption study in Section 6.1, we estimated $\Theta_{crit} = 0.35$ ML. (We mention that an alternative interpretation of the $\Delta\varphi$ data is also possible: initially produced subsurface oxygen, which usually reduces the work function (see, for example, Refs. [Ga77, Ho79a, Mi80, He89, Bo96, Bö99, Ki01]), may, with increasing temperature, segregate to empty on-surface sites and thereby cause the work function increase.)

The UP spectra in Figs. 6.11 and 6.12 show similar features for chemisorbed oxygen ($\Theta \leq 1$ ML or $T_{des} \geq 500$ K) and gold oxide ($\Theta > 1$ ML or $T_{des} < 500$ K), which may also indicate that the former consists of O atoms which are condensed to oxide-like aggregates even at submonolayer coverages. However, the fact that the oxygen-induced emissions depend only very weakly on temperature suggests that the electronic structure of chemisorbed oxygen and gold oxide is very similar, even if no aggregation of the oxygen atoms can occur.

In addition to the here reported similarities in the *electronic structure* between chemisorbed oxygen and gold oxide, Au_2O_3, certain *structural* relations between oxide and chemisorbed species have been discussed in the context of the LEED studies on O/Au(110)-(1×2), which may be of more relevance in this context than the aforementioned UPS results. Several reports have agreed that oxygen chemisorption leads, at monolayer coverage, to a complete suppression of all gold substrate LEED spots due to a disruption of the substrate long-range order. Prolonged annealing close to the desorption temperature did not produce an ordered adsorbate or even substrate structure. The substrate long-range order could only be re-establised through the complete removal of the adsorbate by thermal desorption, sputtering, or reaction with carbon monoxide [Go02, Sa86, Sa98]. This *persistent* disordering effect, which suggests a thermodynamically stable[8] disordered O/Au surface phase, was related to the complicated crystal structure of Au_2O_3 [Jo79], which in turn is likely to be a consequence of convalent contributions to the Au-O bond. The oxygen atoms may demand similar coordination geometries on the surface and in the oxide crystal, which would explain the oxygen-induced disordering of the gold substrate and again confirm the close relationship between chemisorbed oxygen on gold and gold oxide.

[8] This means, there is no ordered structure of lower energy. The O/Au phase can still be metastable relative to the pure elements.

6.7. Appendix: Estimation of the frequency factors by transition state theory (TST)

A desorption order of two, as observed for oxygen adsorption in the low-coverage range, suggests that the rate-limiting step of the desorption process is a bimolecular elementary reaction, viz., the recombination of two O atoms. According to TST [Ey35, Gl41, Ey44], the frequency factor of this reaction is given by:

$$\nu_2 = \kappa \frac{kT}{h} \frac{Q^{\neq}}{Q_O^2} \quad . \qquad \text{(Eq. 6.7)}$$

Reasonable estimations for the partition functions $Q^{\neq}$ (transition state, TS) and Q_O (adsorbed O atoms) enable us to calculate values for the frequency factor ν_2. For the transmission coefficient we assume $\kappa = 1$. In Table 6.2, parallel development of the frequency factors for desorption from the tg-phase (mobile layer) and the tc-phase (immobile layer) are shown. The treatment is similar to that given by Dresser et al. [Dr74] for first-order desorption.

For the (molecular) TS, both translational and rotational partition functions have been taken into account. As usual, all contributions of the vibrational partition functions had to be ignored, since no sufficient information about the respective vibrational frequencies of adsorbate and TS was available. This assumption may introduce a large error, since especially the soft modes (bending, twisting etc.) contribute significantly to the partition function. Unfortunately, exactly these low-frequency modes can usually not be observed in HREELS, since the corresponding signals are obscured by the elastic peak. Therefore, we lack information about the relevant vibrations even for the ground-state adsorbate. Luckily, the error in ν is reduced by a partial cancellation of the vibrational partition functions of ground state and TS. Furthermore, we considered only the partition function of the adsorbed particle, and assumed that the partition function of the substrate surface itself remains unchanged. This may introduce a further error, since a chemisorbed species is likely to influence the vibrational and electronic properties of the substrate and, hence, its partition function.

The mass, $m^{\neq}$, and the momentum of inertia, $I^{\neq}$, of the TS were approximated by the respective values for the O_2 molecule in its vibrational ground state. In the case of immobile adsorption, we distinguish between a partially immobile layer (assuming one rotational and two vibrational degrees of freedom for the TS) and a completely immobile layer with only vibrational degrees of freedom. Due to the above-mentioned simplifications the values of ν obtained in this way should be considered as rough estimates. Not surprisingly, the frequency factor calculated for the tg-phase deviates from the measured value (displayed in Table 6.1) by one order of magnitude.

Two-dimensional gas phase (tg)	Two-dimensional condensed phase (tc)	
Mobile layer (translation, rotation, and vibration)	Partially immobile layer (rotation and vibration)	Completely immobile layer (vibration)
$Q^{\neq} = \left(q_{tr}^{\neq}\right)^2 \, q_{rot}^{\neq} \prod_{i=1}^{3} q_{vib,i}^{\neq}$ $\cong \frac{2\pi m^{\neq} kT}{h^2} \left(\frac{4\pi^2 I^{\neq} kT}{h^2}\right)^{1/2} \prod_{i=1}^{3} \left(1 - e^{-\frac{h\nu_i}{kT}}\right)^{-1}$	$Q^{\neq} = q_{rot}^{\neq} \prod_{i=1}^{5} q_{vib,i}^{\neq}$ $\cong \left(\frac{4\pi^2 I^{\neq} kT}{h^2}\right)^{1/2} \prod_{i=1}^{5} \left(1 - e^{-\frac{h\nu_i}{kT}}\right)^{-1}$	$Q^{\neq} = \prod_{i=1}^{6} q_{vib,i}^{\neq} = \prod_{i=1}^{6} \left(1 - e^{-\frac{h\nu_i}{kT}}\right)^{-1}$
$Q_O = \left(q_{tr,O}\right)^2 \, q_{vib,O} \cong \frac{2\pi m_O kT}{h^2} \left(1 - e^{-\frac{h\nu}{kT}}\right)^{-1}$	$Q_O = \prod_{i=1}^{3} q_{vib,i} = \prod_{i=1}^{3} \left(1 - e^{-\frac{h\nu_i}{kT}}\right)^{-1}$	$Q_O = \prod_{i=1}^{3} q_{vib,i} = \prod_{i=1}^{3} \left(1 - e^{-\frac{h\nu_i}{kT}}\right)^{-1}$
$\nu_{tg} \cong 9.2 \times 10^{-4} \, \frac{cm^2}{s}$	$\nu_{tc} \cong 1.32 \times 10^{14} \, \frac{1}{s \cdot ML}$ equiv. to $0.078 \, \frac{cm^2}{s}$	$\nu_{tc} \cong 1.15 \times 10^{13} \, \frac{1}{s \cdot ML}$ equiv. to $6.8 \times 10^{-3} \, \frac{cm^2}{s}$

Table 6.2: Frequency factors for tg- and tc-phase as estimated by transition state theory. The values given in the bottom line were calculated for T = 550 K by neglection of the vibrational contributions ($q_{vib} \equiv 1$). A transmission coefficient of $\kappa \equiv 1$ was assumed.